JOTCS A
Journal of the Turkish Chemical Society
Section: A
Chemistry
TURKISH CHEMICAL SOCIETY

Structural and Dielectric Properties of RE^{3+}, B^{3+} co-doped (RE^{3+}=Sm^{3+}, Dy^{3+}) $BaTa_2O_6$ Tetragonal Tungsten Bronze-Type Ceramics

Mustafa İlhan[1*], Mehmet İsmail Katı[2], Lütfiye Feray Güleryüz[3]

[1]Department of Environmental Engineering, Faculty of Engineering, Marmara University, Maltepe, 34854, İstanbul, Türkiye.
[2]Department of Medical Imaging Techniques, Vocational School of Health Sciences, Manisa Celal Bayar University, 45030, Manisa, Türkiye.
[3]Department of Tobacco Technology Engineering, Manisa Celal Bayar University, Akhisar 45200, Manisa, Türkiye.

Abstract: In this paper, the effect of boron doping on dielectric properties was investigated using $BaTa_2O_6$:$x$$Sm^{3+}$, $y$$B^{3+}$ (x=5 mol%, y= 0, 5, 15, 30, 50, 70, 100 mol%) and $BaTa_2O_6$:$x$$Dy^{3+}$, y$B^{3+}$ (x=10 mol%, y= 0, 5, 15, 30, 50, 70, 100 mol%) tungsten bronze ceramics fabricated by the conventional solid-state synthesis. XRD (X-ray diffraction) results revealed a single $BaTa_2O_6$ phase with space group *P*4/*mbm* (127) for both series. Additionally, in both series, there was an increase in crystallite sizes and cell parameters with increasing B^{3+} concentration. SEM (scanning electron microscopy) examinations indicated that the increase of boron promoted grain growth and grain elongation. In impedance results, in both series, increasing boron concentration up to 100 mol% increased the dielectric constant. Moreover, the presence of boron was associated with a relaxing transition in the B-site substitution of RE^{3+} (RE=Sm, Dy) ions and a contribution to the dielectric permittivity, while the increase in tetragonality or c/a ratio for both series was ascribed to the increase in the ferroelectric Curie temperature. In both series, a decrease in dielectric loss (tan δ) occurred, which was explained by the increasing sintering temperature effect with increasing boron, reducing the mobility of oxygen vacancies.

Keywords: XRD, SEM, RE^{3+} B^{3+} co-doping, Dielectric properties.

Submitted: March 16, 2024. **Accepted:** May 27, 2024.

Cite this: İlhan M, Katı MI, Güleryüz LF. Structural and Dielectric Properties of RE^{3+}, B^{3+} co-doped (RE^{3+}=Sm^{3+}, Dy^{3+}) $BaTa_2O_6$ Tetragonal Tungsten Bronze-Type Ceramics. JOTCSA. 2024;11(3): 1111-24.

DOI: https://doi.org/10.18596/jotcsa.1453941

***Corresponding author's E-mail:** mustafa.ilhan@marmara.edu.tr

1. INTRODUCTION

Tetragonal tungsten bronze (TTB) oxides compose the largest dielectric family just next to the perovskites (AMO_3), and they exhibits chemical and magnetic stability with excellent crystal structure (1-4). TTB structures can generally have very important and advantageous electrical, magnetic, optical and photocatalytic properties with various applications in the electronics, chemistry and energy conversion areas. Therefore, research on the electrical properties of TTB materials will contribute significantly to the development of multifunctional optoelectronic devices in the future (5-8). Luminescent-ferroelectrics can be obtained from ferroelectric host materials doped with RE ions. Among trivalent rare earths (RE^{3+}), when doped into various inorganic hosts, Sm^{3+} ions exhibit 4f–4f transitions mainly from the $^4G_{5/2}$ excited state to $^6H_{5/2}$, $^6H_{7/2}$, $^6H_{9/2}$, and $^6H_{11/2}$ energy levels, leading to the orange-red emission (9,10), while Dy^{3+} ions show energy levels of $^6H_{15/2}$, $^6H_{13/2}$, $^6H_{11/2}$, and $^6H_{9/2}$ mainly resulting from $^4F_{9/2}$ excitation, leading to blue-yellow-red emission (11-13).

TTB crystal symmetry can be derived from an A-cationic deficient perovskite structure by cylindrical rotation of a square group consisting of four corner-sharing octahedra through 45°, and they may exhibit large spontaneous polarization and high dielectric constants due to its structure consisting of corner-sharing MO_6 (M=Ta, Nb etc) octahedra arrays and three different tunnels (or sites) for cation filling (14-16). $BaTa_2O_6$ exhibits excellent ferroelectric properties, and it has orthorhombic, tetragonal and hexagonal polymorphs, in which the tetragonal polymorph has TTB-type structure (17,18). $BaTa_2O_6$ is reported due to luminescence, dielectric, thermodynamic, and photocatalytic properties (19-22). Boron is widely used to reduce the sintering temperature of ceramics and to improve optical and dielectric properties as well as structural features

such as morphology and crystallinity (23-26). Moreover, there are studies on the effect of boron on grain morphology and its improvement in dielectric properties in which the doping of boron has the effect of increasing the bulk properties to some extent and can reduce the grain boundaries in the structure (27-29).

In the study, the structural and dielectric properties of Sm^{3+}, B^{3+} co-doped $BaTa_2O_6$ and Dy^{3+}, B^{3+} co-doped $BaTa_2O_6$ ceramics were investigated. The structural and dielectric characterizations of the samples were carried out by XRD, SEM, and impedance analyses.

2. EXPERIMENTAL

$BaTa_2O_6$:*x*Sm^{3+}, *y*B^{3+} (*x*=5 mol%, *y*=0, 5, 15, 30, 50, 70 and 100 mol%) and $BaTa_2O_6$:*x*Dy^{3+}, *y*B^{3+} (*x*=10 mol%, *y*=0, 5, 15, 30, 50, 70 and 100 mol%) ceramic samples were fabricated by solid-state reaction. Barium carbonate $BaCO_3$ (Sigma-Aldrich, 99%), niobium oxide (Nb_2O_5: Alfa Aesar, 99.9%), and tantalum oxide (Ta_2O_5: Alfa Aesar, 99.9%) powders were used as starting materials in calculated stoichiometric amounts. Dysprosium oxide (Dy_2O_3: Alfa Aesar, 99.9%) samarium oxide (Sm_2O_3: Alfa Aesar, 99.9%) and boric acid (H_3BO_3: Kimyalab, %99.9) were used as dopant materials. The stoichiometric amounts of $BaTa_2O_6$:0.05Sm^{3+} and $BaTa_2O_6$:0.10Dy^{3+} starting materials were weighed and mixed in an agate mortar to provide homogeneity. Then, by adding different amounts of boric acid (H_3BO_3), the final mixture of the powders was thoroughly mixed and ground in an agate mortar for the last time to provide more homogeneity. For sintering process, the sufficient amount of mixture was taken an alumina crucible at 1425 °C for 10 h after pelleting.

The phase structure of the ceramic samples were examined by (X-ray diffractometer; Panalytical Emperial, Malvern Panalytical Ltd., United Kingdom) using Cu-K_α (1.5406 Å) radiation in between 2θ=20-65 °C with scan speed 2 °C/min. The grain morphology of the ceramic samples was investigated by scanning electron microscopy (FE-SEM; Gemini 500, Zeiss Corp., Germany). The lattice parameters were found from (001) and (400) reflections. The average crystallite sizes were calculated using (101), (210), and (311) reflections from Scherrer Eq. (1) (30):

$$D=\frac{k\cdot\lambda}{B\cdot\cos\theta} \quad (2)$$

where *D* stands for particle size in nanometers, with k assumed to be a constant (usually taken as 0.9). CuKα represents the wavelength (λ = 0.15406 Å), and *B* is the full width at half maximum in radians. Frequency-dependent changes of real and imaginary permittivity and loss factor were defined using dielectric Eq. (2) and Eq. (3) respectively:

$$\varepsilon'=\frac{C}{C_0},\varepsilon''=\frac{G}{\omega C_0},C_0=\varepsilon_0\frac{A}{d} \quad (2)$$

$$tan\delta=\frac{\varepsilon''}{\varepsilon'} \quad (3)$$

where C_0 is vacuum capacitance, *C* is capacitance, *w* is angular frequency and *G* is conductance. The dielectric properties of the ceramic samples were carried out using an impedance analyzer (HIOKI, LCR Hitester 3532-50; between frequency 20 Hz–10^6 Hz, UK) at room temperature.

3. RESULTS AND DISCUSSION

3.1. XRD-SEM Results of $BaTa_2O_6$:*x*Sm^{3+}, *y*B^{3+} and $BaTa_2O_6$:*x*Dy^{3+}, *y*B^{3+} Ceramics

Figure 1 and Figure 2 show the XRD results for $BaTa_2O_6$:*x*Sm^{3+}, *y*B^{3+} (*x*=5 mol%, *y*=0, 5, 15, 30, 50, 70 and 100 mol%) and $BaTa_2O_6$:*x*Dy^{3+}, *y*B^{3+} (*x*=10 mol%, *y*=0, 5, 15, 30, 50, 70 and 100 mol%) series, respectively. In both series, X-ray diffractions of all the sintered samples from 0 to 100 mol% B^{3+} have $BaTa_2O_6$ pattern. The single-phase TTB (tetragonal tungsten bronze) type structure of $BaTa_2O_6$ identified by XRD peaks JCPDS card no. 17-0793 and *P4/mbm* (127) space group (9,10).

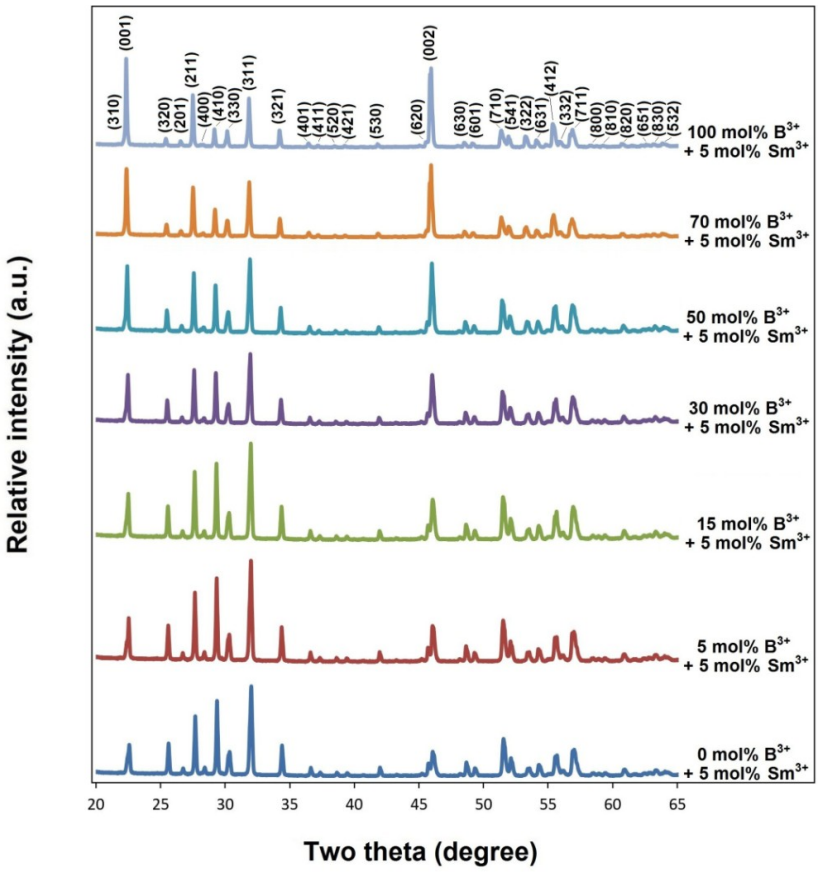

Figure 1: X-ray diffractions of $BaTa_2O_6$:$x$$Sm^{3+}$, $y$$B^{3+}$ (x=5 mol%, y= 0, 5, 15, 30, 50, 70 and 100 mol%) ceramic series.

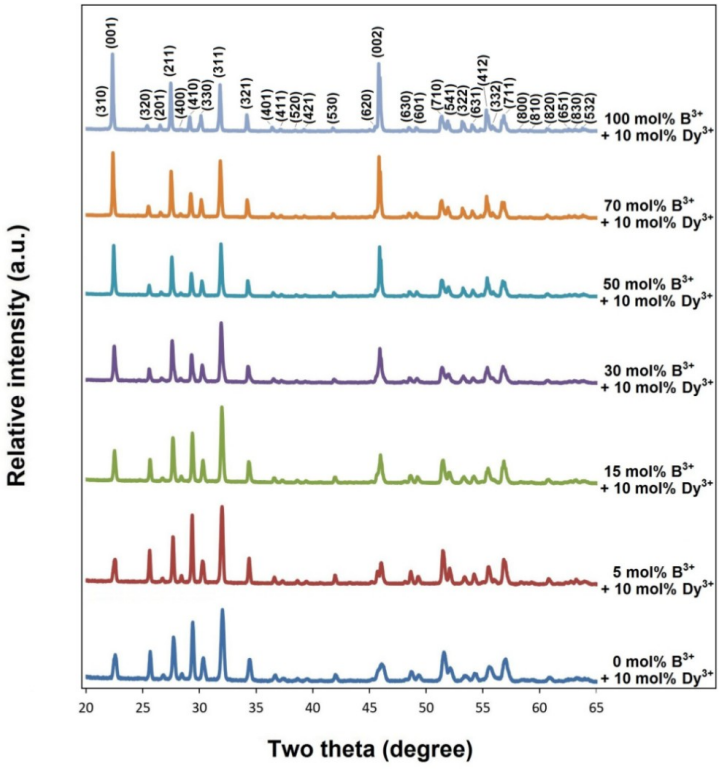

Figure 2: X-ray diffractions of $BaTa_2O_6$:$x$$Dy^{3+}$, $y$$B^{3+}$ (x=10 mol%, y= 0, 5, 15, 30, 50, 70 and 100 mol%) ceramic series.

Figure 3 shows the schematic view of TTB-$BaTa_2O_6$ structure expressed with the formula $A_4B_2C_4M_{10}O_{30}$. Accordingly, A tunnels are pentagonal with a coordination number (CN) of 15, the B tunnels are square with a CN of 12, and the C tunnels are triangular with a CN of 9, while the octahedral Ta sites in the structure have a CN of 6 (19,24). In addition, as seen in Figure 3, the $BaTa_2O_6$ is composed of a structure of adjacent octahedral-sharing corners where the pentagonal A sites are occupied by Ba^{2+}, the square B sites by Ba^{2+} or empty, and the small triangular (C) sites are empty, where Ba^{2+} cations have ionic radii of 1.61 Å for 12 CN, and 1.47 Å for 9 CN. Based on the suitability of sites A and B for RE^{3+} (RE=Sm, Dy) occupation, for Sm^{3+} ions (r=1.24 Å for CN 12 and r=1.132 Å for CN 9) and Dy^{3+} (r=1.083 Å for CN 9) ions will be able to occupy the A and B sites, respectively. Consequently, the absence of a secondary phase in the XRD peaks for the 5 mol% Sm^{3+} doped series and the 10 mol% Dy^{3+} doped series showed that RE^{3+} ions were incorporated in the A and B sites as interstitial atoms in the structure. Moreover, the absence of a secondary phase indicated that B^{3+} ions were dissolved in the three-tunnel structure of $BaTa_2O_6$. Similar results have been reported in the study on the luminescence of β-$SrTa_2O_6$:Eu^{3+}, B^{3+}, and XPS results confirm that boron is incorporated in the tungsten bronze structure (23). On the other hand, as seen in Figure 1 and Figure 2, increasing B^{3+} concentration caused an increase in (001) and (002) peaks. In the study reported by Gardner and Morrison (31), the increased splitting in (001) reflections and the B-site cation size RE (RE = La, Nd, Sm, Gd, Dy, Y) decreases. Additionally, in luminescence on $BaTa_2O_6$:Eu^{3+}, B^{3+} phosphor conducted by İlhan et al (24), the (001) reflection increases with the increase in B^{3+}, while the asymmetry ratio, which is related to increased Eu^{3+} activation in B sites, decreases. This issue will be discussed in detail in the dielectric section.

The cell data and crystallite sizes of $BaTa_2O_6$:$x$$Sm^{3+}$, $y$$B^{3+}$ and $BaTa_2O_6$:$x$$Dy^{3+}$, $y$$B^{3+}$ series are tabulated in Table 1 and Table 2, respectively. The lattice parameters from 0 to 100 mol% B^{3+} changed to a=12.5544 Å, c=3.9377 Å, V=620.64 Å^3, and a=12.6151 Å, c=3.9799 Å, V=633.37 Å^3 (for $BaTa_2O_6$:$x$$Sm^{3+}$, $y$$B^{3+}$); a=12.5427 Å, c=3.9377 Å, V=619.48 Å^3, and a=12.6049 Å, c=3.9798 Å, V=632.33 Å^3 (for $BaTa_2O_6$:$x$$Dy^{3+}$, $y$$B^{3+}$) respectively. The cell parameters of tetragonal $BaTa_2O_6$ are reported as a=12.52 Å, b= 3.956 Å, V=620.10 Å^3 by Layden (18), and it appears the lattice data in the study are compatible with the literature. In addition, the c/a ratio, which expresses tetragonality, decreased with increasing B^{3+} concentration in both series. In Table 1 and Table 2, the c/a ratios for the $BaTa_2O_6$:$x$$Sm^{3+}$, $y$$B^{3+}$ and $BaTa_2O_6$:$x$$Dy^{3+}$, $y$$B^{3+}$ series were found 0.3137-0.3155 and 0.3139-0.3157 for 0 and 100 mol% B^{3+}, respectively. The increase in boron led to an increase in crystallite size, while the sizes changed to 33.54-50.30 nm (for $BaTa_2O_6$:$x$$Sm^{3+}$, $y$$B^{3+}$) and 30.05-48.71 nm (for $BaTa_2O_6$:$x$$Dy^{3+}$, $y$$B^{3+}$) from 0 to 100 mol% B^{3+}, respectively. Since the temperature effect will increase with the increase of boron and the nucleation rate will slow down, therefore the increase in crystal size can be attributed to the decrease in nucleation and also the change in the charge balance of cell.

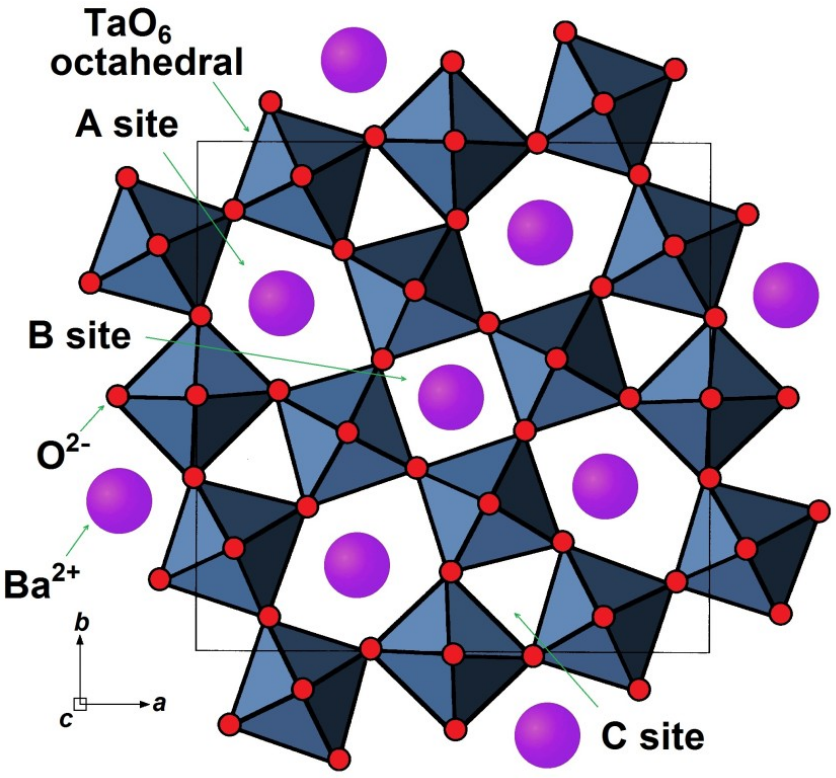

Figure 3: Schematic illustration of TTB-$BaTa_2O_6$ crystal structure.

Table 1: Cell parameters and average crystallite sizes for $BaTa_2O_6$: $x$$Sm^{3+}$, $y$$B^{3+}$ ceramics.

Sample (mol%)	Lattice parameters				Crystallite size (*D*) (nm)
	a **(Å)**	***c*** **(Å)**	***V*** **(Å³)**	***c/a***	
0 B^{3+}, 5 Sm^{3+}	12.5544	3.9377	620.64	0.3137	33.54
5 B^{3+}, 5 Sm^{3+}	12.5654	3.9445	622.79	0.3139	35.41
15 B^{3+}, 5 Sm^{3+}	12.5711	3.9491	624.08	0.3141	37.49
30 B^{3+}, 5 Sm^{3+}	12.5825	3.9536	625.93	0.3142	39.83
50 B^{3+}, 5 Sm^{3+}	12.5939	3.9627	628.52	0.3147	42.48
70 B^{3+}, 5 Sm^{3+}	12.6111	3.9745	632.10	0.3152	45.51
100 B^{3+}, 5 Sm^{3+}	12.6151	3.9799	633.37	0.3155	50.30

Table 2: Cell parameters and average crystallite sizes for $BaTa_2O_6$: $x$$Dy^{3+}$, $y$$B^{3+}$ ceramics.

Sample (mol%)	Lattice parameters				Crystallite size (*D*) (nm)
	a **(Å)**	***c*** **(Å)**	***V*** **(Å³)**	***c/a***	
0 B^{3+}, 10 Dy^{3+}	12.5427	3.9377	619.48	0.3139	30.05
5 B^{3+}, 10 Dy^{3+}	12.5540	3.9402	620.98	0.3139	31.82
15 B^{3+}, 10 Dy^{3+}	12.5654	3.9468	623.15	0.3141	34.65
30 B^{3+}, 10 Dy^{3+}	12.5825	3.9513	625.57	0.3140	39.97
50 B^{3+}, 10 Dy^{3+}	12.5882	3.9605	627.58	0.3146	42.13
70 B^{3+}, 10 Dy^{3+}	12.5996	3.9719	630.54	0.3152	44.54
100 B^{3+}, 10 Dy^{3+}	12.6049	3.9798	632.33	0.3157	48.71

Figure 4(a-g) and Figure 5(a-g) show the SEM micrographs of $BaTa_2O_6$:$x$$Sm^{3+}$, $y$$B^{3+}$ (x=5 mol%, y=0, 5, 30, 50, 70, 100 mol%) and $BaTa_2O_6$:$x$$Dy^{3+}$, $y$$B^{3+}$ (x=10 mol%, y=0, 5, 30, 50, 70, 100 mol%) samples, respectively, at 2000× magnifications under 2 kV accelerating voltage. In the SEM micrographs of both series, grains were shapless and roundish at low B^{3+} concentration, while increasing boron concentration caused grain growth and rod-like shape in grains. As is well known, boron has a reducing effect on the sintering temperature due to the flux effect. Therefore, the increase in grain size can be explained by the increasing temperature effect of boron addition, which releases the energy stored in the grains and thus causes the grain size to increase (32,33). In Figure 4a and Figure 5a, the undoped B^{3+} samples have a small grain size and a round-like irregular grain-shaped morphology in both series. For $BaTa_2O_6$:$x$$Sm^{3+}$, $y$$B^{3+}$ series, in Figure 4b, the grains to grow and elongate began to occur in the sample co-doped with 5 mol% B^{3+}, and it became more pronounced at 15 mol% B^{3+} (Figure 4c). In Figure 4d, the grain shape of the 30 mol% B^{3+} doped sample had almost rod-like, and showing thick-grain formations while the growth and elongation trend in the grains continued as seen in Figure 4(e-g). In Figure 4e, the fine grain morphology was considerably decreased at 50 mol % B^{3+}, and it completely disappeared at 70 (Figure 4f) and 100 mol% (Figure 4g) B^{3+} concentrations. For $BaTa_2O_6$:$x$$Dy^{3+}$, $y$$B^{3+}$ series, similar to the $BaTa_2O_6$:$x$$Sm^{3+}$, $y$$B^{3+}$ series in Figure 5b, grain growth occurred in the sample doped with 5 mol% B^{3+}, while it continued at 15 (Figure 5c), 30 (Figure 5d), 50 (Figure 5e), 70 (Figure 5f), and 100 (Figure 5g) mol%. Also, thickening was evident in the $BaTa_2O_6$:$x$$Dy^{3+}$, $y$$B^{3+}$ series. The grain sizes for the undoped B^{3+} sample usually range of 0.2-1.5 μm (for $BaTa_2O_6$:$x$$Sm^{3+}$, $y$$B^{3+}$) and 0.3-3 μm (for $BaTa_2O_6$:$x$$Dy^{3+}$, $y$$B^{3+}$). The thicknesses and lengths at 100 mol% reached the range of 2-15 μm and 5-40

μm (for $BaTa_2O_6$:$x$$Sm^{3+}$, $y$$B^{3+}$) and 2.5-30 μm and 6-50 μm (for $BaTa_2O_6$:$x$$Dy^{3+}$, $y$$B^{3+}$), respectively.

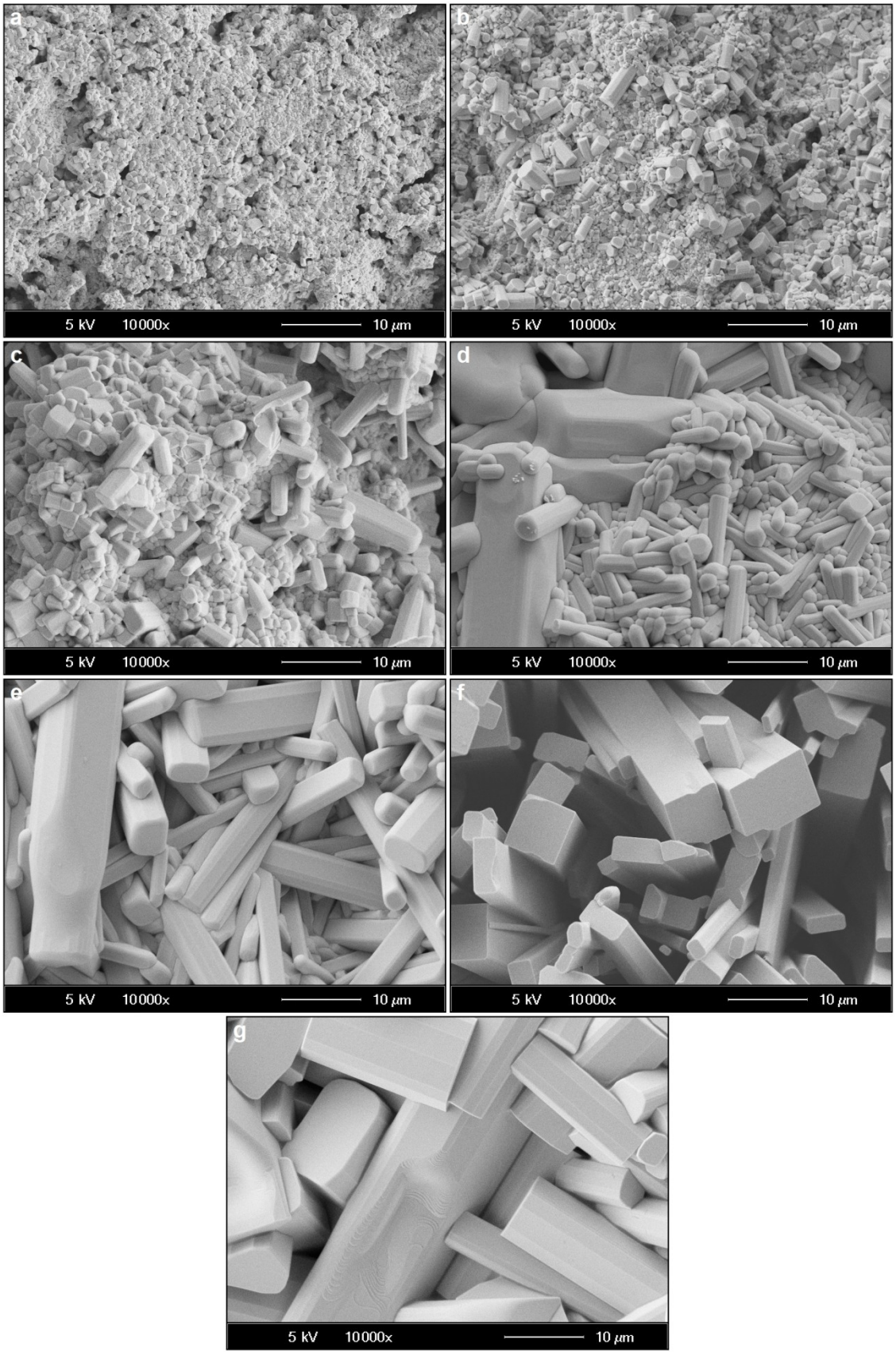

Figure 4: SEM micrographs of 5 mol% Sm^{3+} and (a) 0, (b) 5, (c) 15, (d) 30, (e) 50, (f) 70 and (g) 100 mol% B^{3+} co-doped $BaTa_2O_6$ ceramics, at 10000× magnification and 5 kV acceleration voltage.

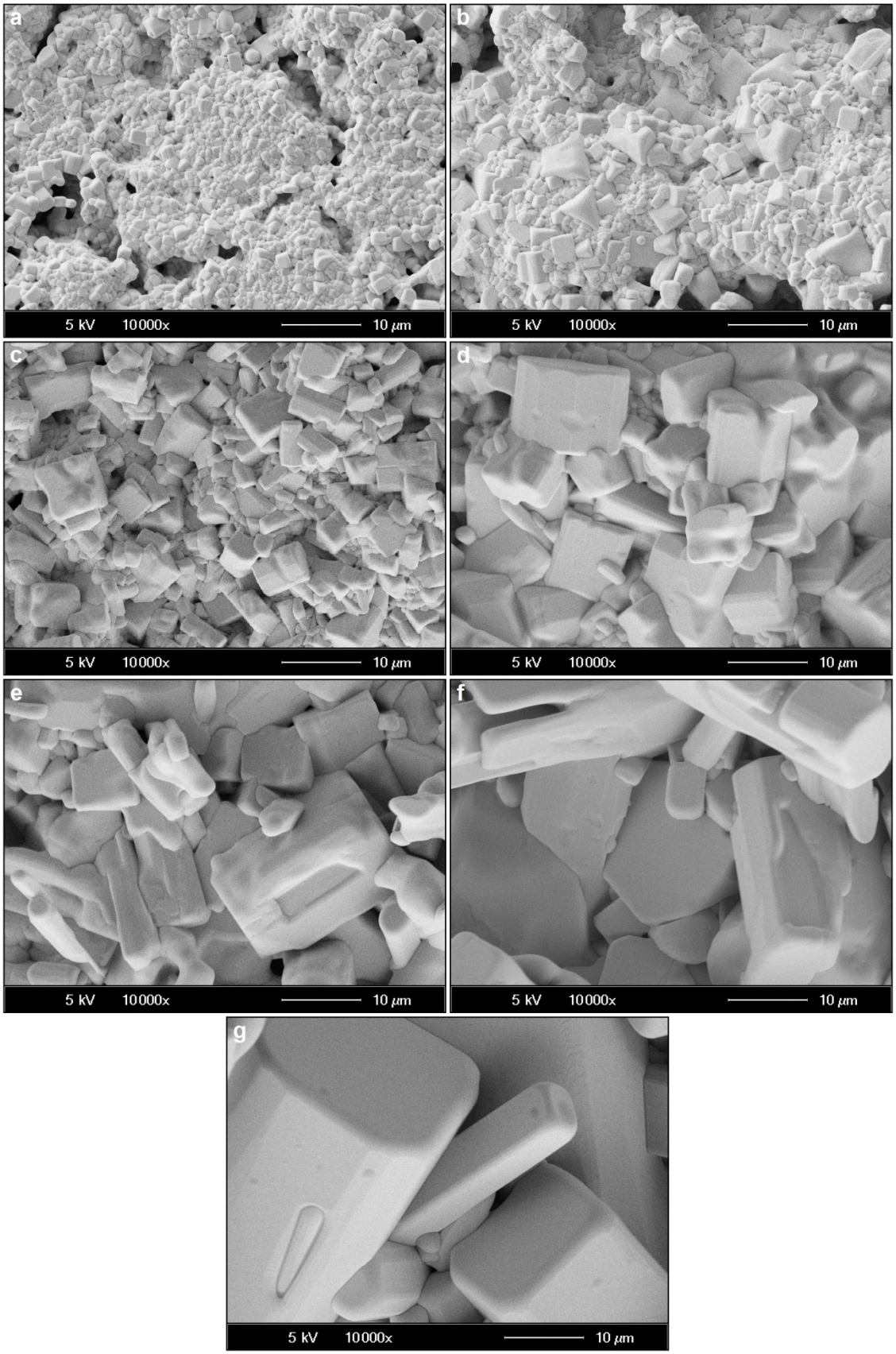

Figure 5: SEM micrographs of 10 mol% Dy^{3+} and (a) 0, (b) 5, (c) 15, (d) 30, (e) 50, (f) 70 and (g) 100 mol% B^{3+} co-doped $BaTa_2O_6$ ceramics, at 10000× magnification and 5 kV acceleration voltage.

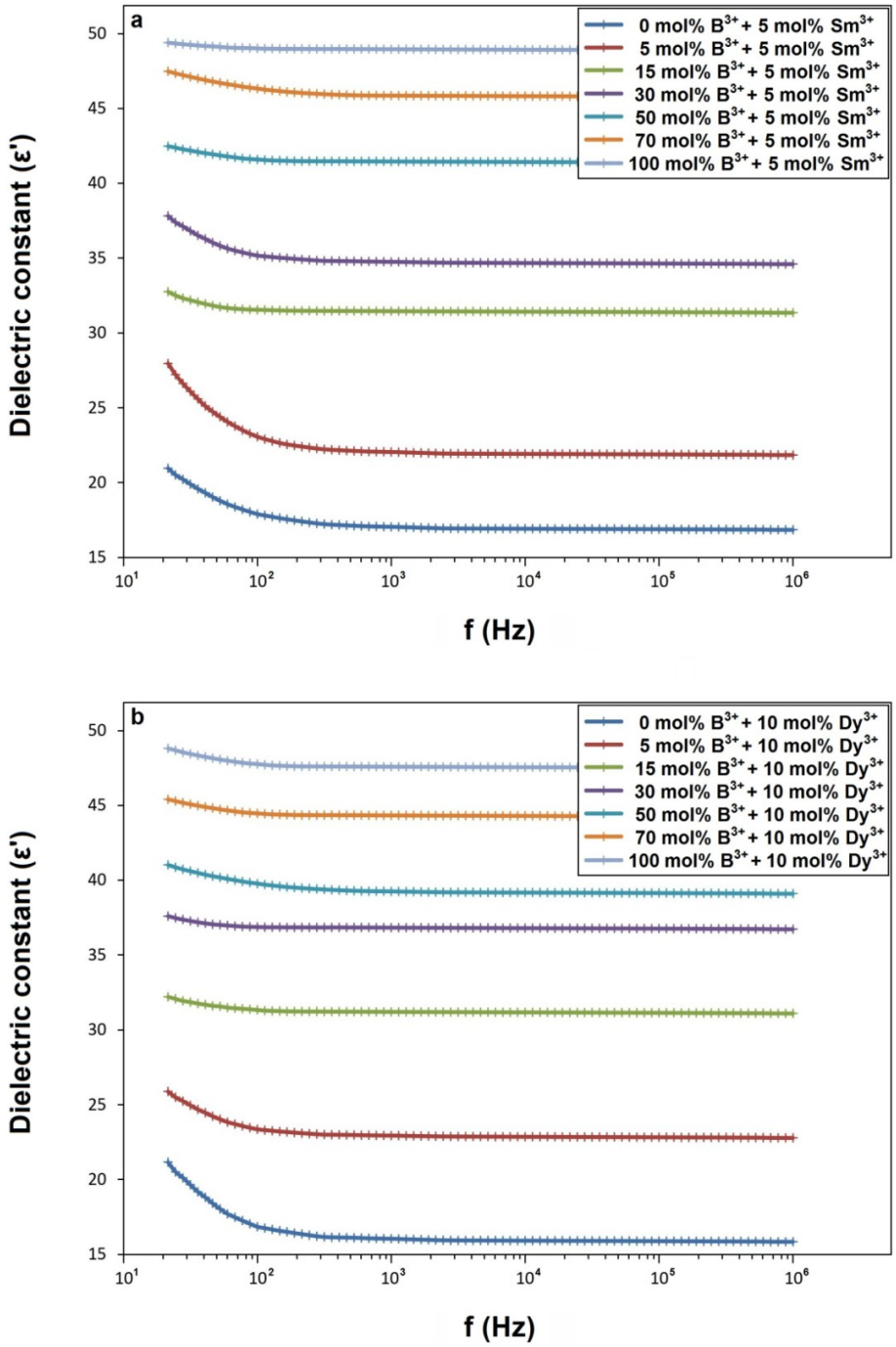

Figure 6: Dielectric constants (ε') for (a) $BaTa_2O_6$:$x$$Sm^{3+}$, y$B^{3+}$ (x=5 mol%, y=0, 5, 15, 30, 50, 70, 100 mol %), and (b) $BaTa_2O_6$:$x$$Dy^{3+}$, y$B^{3+}$ (x=10 mol%, y=0, 5, 15, 30, 50, 70, 100 mol%) ceramics.

3.2. Dielectric Properties of $BaTa_2O_6$:$x$$Sm^{3+}$, $y$$B^{3+}$ and $BaTa_2O_6$:$x$$Dy^{3+}$, $y$$B^{3+}$ Series

Figure 6(a,b) show the dielectric constants (ε') with frequency for $BaTa_2O_6$:$x$$Sm^{3+}$, $y$$B^{3+}$ (x=5 mol%, y=0, 5, 15, 30, 50, 70 and 100 mol%) and $BaTa_2O_6$:$x$$Dy^{3+}$, $y$$B^{3+}$ (x=10 mol%, y=0, 5, 15, 30, 50, 70 and 100 mol%) samples, respectively. In Figure 6a, the dielectric constants of $BaTa_2O_6$:$x$$Sm^{3+}$, $y$$B^{3+}$ series from 0 to 100 mol% B^{3+} changed approximately 21.1 and 49.4 at 20 Hz, respectively. In Figure 6b, at the same range and 20 Hz, the ε' values for the $BaTa_2O_6$:$x$$Dy^{3+}$, $y$$B^{3+}$ series were 21.3 and 48.9, respectively. However, the dielectric constant did not change in the high frequency or over 10^3 Hz. As the frequency increases, the ability of electron exchange to follow the applied field decreases, and thus the dielectric constant decreases. At very high frequencies, the field reverses before the movement of space charge carriers, and as a result, it does not contribute to polarization (34-40), so the dielectric constant almost stayed unchanged at the high-frequency range. Moreover, as seen in Figure 6(a,b) there is an increase in polarization or dielectric constant from 0 to 100 mol% B^{3+} in both series This increase may be explained based on Maxwell-Wagner external factors theory (41,42). According

to this theory, the dielectric constant is directly proportional to the grain size of the sample, where an increase in grain size leads to an increase in the polarizability of the atoms, and causes an increase in dielectric constant (41-45). In the SEM micrographs in Figure 4(a-g) and Figure 5(a-g), it was previously noted that there is an increase in grain size with increasing B^{3+} concentration. Therefore, this situation may be explained by the decreasing presence of the grain boundaries in both series, and thus the increase in the polarizability and ε' value of the atoms in the structure. Moreover, in Table 1 and Table 2, the enhancing crystalline sizes support the improvement in bulk property and increase in dielectric constant (46,47). On the other hand, as highlighted in many studies, TTB-type compounds can be expected to contribute to paraelectric behavior due to their ferroelectric properties. In the studies, it has been shown that centrosymmetric B-site substitution affects the ferroelectric properties of TTB compounds where the A-site size is fixed (48-50). The B-site substitution can lead to a relaxor transition and improve the dielectric permittivity, indicating that B-site substitution is an excellent method to improve the dielectric properties of TTB (31,51). As is well known, the $^5D_0 \rightarrow {}^7F_2$ transition in Eu^{3+} luminescence is a “hypersensitive transition” and provides information about the environmental symmetry of the Eu^{3+} ion. In this context, the non-centrosymmetric A-sites and centrosymmetric B-sites in TTB structure are related to the $^5D_0 \rightarrow {}^7F_2$ and $^5D_0 \rightarrow {}^7F_1$ transitions of Eu^{3+}, respectively. So, the $^5D_0 \rightarrow {}^7F_2/{}^5D_0 \rightarrow {}^7F_1$ ratio or asymmetry ratio indicates the occupancy of A and B sites where decreasing ratio is associated with the B-site (24,52). Relatedly, the structural, morphological and luminescence properties $BaTa_2O_6$:$x$$Eu^{3+}$, $y$$B^{3+}$ (x=10 mol%, y=0, 5, 15, 30, 50, 70, and 100 mol%) phosphors are studied, in which the asymmetry ratio decreased approximately 70% up to 100 mol% boron concentration, indicating Eu^{3+} activation in B sites (24). Moreover, the structural and morphological results of $BaTa_2O_6$:$x$$Eu^{3+}$, $y$$B^{3+}$ show close similarities to the Sm^{3+} and Dy^{3+} ions examined in this study. Consequently, it is possible that boron concentration shows a similar behavior for Sm^{3+} and Dy^{3+} ions in tungsten bronze structure, causing a relaxing transition in B site substitution and contributing to the dielectric permeability. Furthermore, regarding TTB structures in relation to B-site occupation, there are some papers on Curie temperature (T_C) and c/a ratio (tetragonality). Gardner and Morrison (31) highlighted the ferroelectric Curie temperature (T_C) for the TTB-$Ba_4R_{0.67}Nb_{10}O_{30}$ (R = La, Nd, Sm, Gd, Dy, Y) increases with the increase in tetragonality, and RE cation size is decreasing. Similarly, Stennett et al (51) reported an increase in Curie temperature with decreasing ionic radius M in the B-site of TTB-$Ba_2MTi_2Nb_3O_{15}$ (M=Bi, La, Pr, Nd, Sm, Eu, Gd, Dy), in which tetragonality increases. As seen in Table 1 and Table 2, the c/a ratio of both series increased up to 100 mol% B^{3+} concentration. According to these findings, the increase in B^{3+} availability resulting in an increase in tetragonality may be linked to an increase in the ferroelectric Curie temperature. Moreover, in Table 1 and Table 2, when the c/a ratios are compared, the c/a ratios of the Dy^{3+} cation with a smaller ionic radius are relatively high. Thus, a decreasing radius indicates increasing tetragonality and Curie temperature, which is in agreement with References (31) and (51).

Figure 7(a,b) show the dielectric losses (tan δ) with frequency for $BaTa_2O_6$:$x$$Sm^{3+}$, $y$$B^{3+}$ (x=5 mol%, y=0, 5, 15, 30, 50, 70 and 100 mol%) and $BaTa_2O_6$:$x$$Dy^{3+}$, $y$$B^{3+}$ (x=10 mol%, y=0, 5, 15, 30, 50, 70 and 100 mol%) samples, respectively. In Figure 7a, the dielectric loss of $BaTa_2O_6$:$x$$Sm^{3+}$, $y$$B^{3+}$ series from 0 to 100 mol% B^{3+} changed approximately 0.40 and 0.02 at 20 Hz, respectively. In Figure 7b, at the same range and 20 Hz, the ε' values for the $BaTa_2O_6$:$x$$Dy^{3+}$, $y$$B^{3+}$ series were 0.45 and 0.01, respectively. Additionally, both series exhibited a dielectric loss below approximately 0.10 in the range of 5-100 mol% and at 20 Hz. In Figure 7(a,b), the dielectric loss decreases continuously as the frequency increases. In the low frequency range corresponding to high resistance, more energy is required for polarization due to the grain boundary, whereas in the high frequency range corresponding to low resistance, very little energy will be needed for electron transfer due to the grain boundary, and the energy loss will be less (53,54). Moreover, the dielectric loss factor for both sample series decreases with increasing B^{3+}. In the literature, different studies highlight oxygen vacancies as responsible for dielectric loss or leakage current in ferroelectrics (55-61). In the study of Kumar and Kar (55), the substitution of Ti^{4+} into $BiFeO_3$ significantly reduces oxygen vacancies and leakage current for tan δ. Similarly, Sati et al (56) attributed the decreased dielectric loss with Eu substitution to $BiFeO_3$ to the decrease in oxygen vacancies. Liu et al (57) investigated the dielectric loss and oxygen vacancy relation by fabricating TTB-$Ba_4Nd_2Fe_2Nb_8O_{30}$ ceramics at different annealing and sintering temperatures as well as in O_2 and N_2 atmospheres, in which the increase in temperature reduces oxygen vacancies and electrical conductivity. The consequences of the temperature effect resulting from the increase in boron were mentioned in the structural section. In this context, the increased boron concentration will not only cause a greater temperature effect on the material, but also have an effect on oxygen vacancies. Consequently, the decrease in the dielectric loss factor in both series may be attributed to the suppression of oxygen vacancies by the temperature effect that increases with the increase in B^{3+}.

4. CONCLUSION

The effect of boron on the structural and dielectric properties was studied by using Eu^{3+}, B^{3+} co-doped tetragonal tungsten bronze $BaTa_2O_6$:$x$$Sm^{3+}$, $y$$B^{3+}$ (x=5 mol%, y=0, 5, 15, 30, 50, 70, 100 mol%) and $BaTa_2O_6$:$x$$Dy^{3+}$, $y$$B^{3+}$ (x=10 mol%, y=0, 5, 15, 30, 50, 70, 100 mol%) ceramics. The single-phase structure was preserved in XRD results of both series, while the crystallinity of the samples increased with boron concentration. SEM micrographs of Sm^{3+}, B^{3+} co-doped and Dy^{3+}, B^{3+} co-doped samples showed that boron supported grain growth and elongation. The dielectric constants (ε') for $BaTa_2O_6$:$x$$Sm^{3+}$, $y$$B^{3+}$, and $BaTa_2O_6$:$x$$Dy^{3+}$, $y$$B^{3+}$ series were measured in the range of 21.1-49.4 and 21.3-48.9 at 20 Hz, respectively. For both series, the increasing dielectric constant up to 100 mol% B^{3+}

concentration was associated with the improving grain size and crystallinity. The dielectric loss factor for both series decreased with increasing B^{3+} concentration, while the tan δ for $BaTa_2O_6$:$x$$Sm^{3+}$, $y$$B^3$ and $BaTa_2O_6$:$x$$Dy^{3+}$, $y$$B^3$ changed as 0.40-0.02 and 0.45-0.01 at 20 Hz, respectively. The dielectric loss decrease in both series with the increasing B^{3+} concentration was attributed to the suppression of oxygen vacancies with the increased presence of B^{3+}. The study may be useful in evaluating the dielectric properties of tetragonal tungsten bronze ceramics, in terms of controlling the grain morphology and crystallite size.

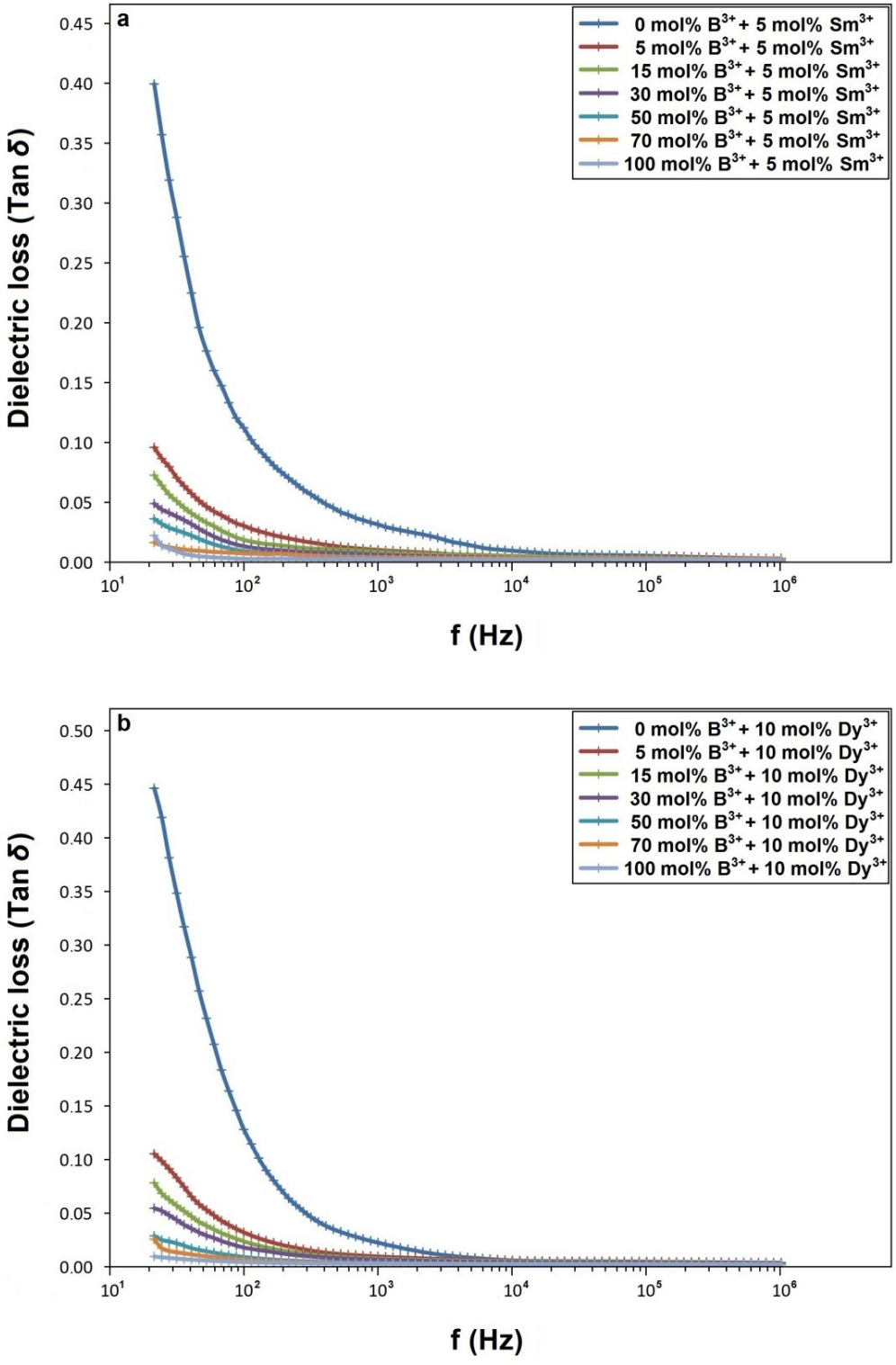

Figure 7: Dielectric losses (tan δ) for (a) $BaTa_2O_6$:$x$$Sm^{3+}$, y$B^{3+}$ (x=5 mol%, y=0, 5, 15, 30, 50, 70, 100 mol %), and (b) $BaTa_2O_6$:$x$$Dy^{3+}$, y$B^{3+}$ (x=10 mol%, y=0, 5, 15, 30, 50, 70, 100 mol%) ceramics.

5. CONFLICT OF INTEREST

There is no conflict of interest

6. REFERENCES

1. Feng W Bin, Zhu XL, Liu XQ, Fu M Sen, Ma X, Jia SJ, et al. Relaxor nature in $Ba_5RZr_3Nb_7O_{30}$ (R= La, Nd, Sm) tetragonal tungsten bronze new system. J Am Ceram Soc [Internet]. 2018 Apr 24;101(4):1623–31. Available from: <URL>.

2. Zhu XL, Liu XQ, Chen XM. Crystal Structure and Dielectric Properties of $Sr_5RTi_3Nb_7O_{30}$ (R=La, Nd, Sm, and Eu) Tungsten Bronze Ceramics. J Am Ceram Soc [Internet]. 2011 Jun;94(6):1829–36. Available from: <URL>.

3. Roulland F, Josse M, Castel E, Maglione M. Influence of ceramic process and Eu content on the composite multiferroic properties of the $Ba_{6-2x}Ln_{2x}Fe_{1+x}Nb_{9-x}O_{30}$ TTB system. Solid State Sci [Internet]. 2009 Sep;11(9):1709–16. Available from: <URL>.

4. Fang L, Peng X, Li C, Hu C, Wu B, Zhou H. Dielectric Properties of $Ba_4Sm_2Fe_2M_8O_{30}$ (M=Nb, Ta) with Tetragonal Bronze Structure. J Am Ceram Soc [Internet]. 2010 Sep 12;93(9):2430–3. Available from: <URL>.

5. Bendahhou A, Marchet P, El-Houssaine A, El Barkany S, Abou-Salama M. Relationship between structural and dielectric properties of Zn-substituted $Ba_5CaTi_{2-x}Zn_xNb_8O_{30}$ tetragonal tungsten bronze. CrystEngComm [Internet]. 2021;23(1):163–73. Available from: <URL>.

6. Botella P, Solsona B, García-González E, González-Calbet JM, López Nieto JM. The hydrothermal synthesis of tetragonal tungsten bronze-based catalysts for the selective oxidation of hydrocarbons. Chem Commun [Internet]. 2007;(47):5040–2. Available from: <URL>.

7. Jindal S, Vasishth A, Devi S, Anand G. A review on tungsten bronze ferroelectric ceramics as electrically tunable devices. Integr Ferroelectr [Internet]. 2018 Jan 2;186(1):1–9. Available from: <URL>.

8. Shimizu K, Kato H, Kobayashi M, Kakihana M. Synthesis and photocatalytic properties of tetragonal tungsten bronze type oxynitrides. Appl Catal B Environ [Internet]. 2017 Jun;206:444–8. Available from: <URL>.

9. İlhan M, Güleryüz LF. Cathodoluminescence and photoluminescence of $BaTa_2O_6$:Sm^{3+} phosphor depending on the sintering temperature. Chem Pap [Internet]. 2022 Nov;76(11):6963–74. Available from: <URL>.

10. Ekmekçi MK, İlhan M, Başak AS, Deniz S. Structural and Luminescence Properties of Sm^{3+} Doped TTB -Type $BaTa_2O_6$ Ceramic Phosphors. J Fluoresc [Internet]. 2015 Nov 26;25(6):1757–62. Available from: <URL>.

11. İlhan M, Keskin İÇ, Gültekin S. Assessing of Photoluminescence and Thermoluminescence Properties of Dy^{3+} Doped White Light Emitter TTB-Lead Metatantalate Phosphor. J Electron Mater [Internet]. 2020 Apr 17;49(4):2436–49. Available from: <URL>.

12. İlhan M, Keskin İÇ. Analysis of Judd–Ofelt parameters and radioluminescence results of $SrNb_2O_6$:Dy^{3+} phosphors synthesized via molten salt method. Phys Chem Chem Phys [Internet]. 2020;22(35):19769–78. Available from: <URL>.

13. Ekmekçi MK, İlhan M, Güleryüz LF, Mergen A. Study on molten salt synthesis, microstructural determination and white light emitting properties of $CoNb_2O_6$:Dy^{3+} phosphor. Optik (Stuttg) [Internet]. 2017 Jan;128:26–33. Available from: <URL>.

14. Tressaud A. Structural architecture and physical properties of some inorganic fluoride series: a review. J Fluor Chem [Internet]. 2011 Oct;132(10):651–9. Available from: <URL>.

15. İlhan M, Ekmekçi MK, Mergen A, Yaman C. Photoluminescence characterization and heat treatment effect on luminescence behavior of $BaTa_2O_6$:Dy^{3+} phosphor. Int J Appl Ceram Technol [Internet]. 2017 Nov 13;14(6):1134–43. Available from: <URL>.

16. İlhan M, Keskin İÇ. Evaluation of the Structural, Near-Infrared Luminescence, and Radioluminescence Properties of Nd^{3+} Activated TTB-Lead Metatantalate Phosphors. J Turkish Chem Soc Sect A Chem [Internet]. 2023 May 31;10(2):453–64. Available from: <URL>.

17. Xu T, Zhao X, Zhu Y. Synthesis of Hexagonal $BaTa_2O_6$ Nanorods and Influence of Defects on the Photocatalytic Activity. J Phys Chem B [Internet]. 2006 Dec 1;110(51):25825–32. Available from: <URL>.

18. Layden GK. Polymorphism of $BaTa_2O_6$. Mater Res Bull [Internet]. 1967 May;2(5):533–9. Available from: <URL>.

19. Keskin İÇ, İlhan M. Thermoluminescence Kinetic Parameters and Radioluminescence of RE^{3+} (RE = Pr, Sm, Tb, Ho, Er)-Doped Barium Tantalate Phosphors. J Electron Mater [Internet]. 2023 Aug 31;52(8):5614–30. Available from: <URL>.

20. Layden GK. Dielectric and structure studies of hexagonal $BaTa_2O_6$. Mater Res Bull [Internet]. 1968 Apr;3(4):349–59. Available from: <URL>.

21. İlhan M, Mergen A, Sarıoğlu C, Yaman C. Heat capacity measurements on $BaTa_2O_6$ and derivation of its thermodynamic functions. J Therm Anal Calorim [Internet]. 2017 May 29;128(2):707–11. Available from: <URL>.

22. Kato H, Kudo A. New tantalate photocatalysts for water decomposition into H_2 and O_2. Chem Phys Lett [Internet]. 1998 Oct;295(5–6):487–92. Available from: <URL>.

23. İlhan M, Güleryüz LF. Boron doping effect on the structural, spectral properties and charge transfer mechanism of orthorhombic tungsten bronze β-

$SrTa_2O_6:Eu^{3+}$ phosphor. RSC Adv [Internet]. 2023;13(18):12375–85. Available from: <URL>.

24. İlhan M, Güleryüz LF, Katı Mİ. Exploring the effect of boron on the grain morphology change and spectral properties of Eu^{3+} activated barium tantalate phosphor. RSC Adv [Internet]. 2024;14(4):2687–96. Available from: <URL>.

25. Başak AS, Ekmekçi MK, Erdem M, Ilhan M, Mergen A. Investigation of Boron-doping Effect on Photoluminescence Properties of $CdNb_2O_6$: Eu^{3+} Phosphors. J Fluoresc [Internet]. 2016 Mar 11;26(2):719–24. Available from: <URL>.

26. İlhan M, Ekmekçi MK, Güleryüz LF. Effect of boron incorporation on the structural, morphological, and spectral properties of $CdNb_2O_6:Dy^{3+}$ phosphor synthesized by molten salt process. Mater Sci Eng B [Internet]. 2023 Dec;298:116858. Available from: <URL>.

27. Zhang X, Wang B, Huang W, Chen Y, Wang G, Zeng L, et al. Synergistic Boron Doping of Semiconductor and Dielectric Layers for High-Performance Metal Oxide Transistors: Interplay of Experiment and Theory. J Am Chem Soc [Internet]. 2018 Oct 3;140(39):12501–10. Available from: <URL>.

28. Mazumder R, Seal A, Sen A, Maiti HS. Effect of Boron Addition on the Dielectric Properties of Giant Dielectric $CaCu_3Ti_4O_{12}$. Ferroelectrics [Internet]. 2005 Oct;326(1):103–8. Available from: <URL>.

29. Li Z, Zhou W, Su X, Luo F, Huang Y, Wang C. Effect of boron doping on microwave dielectric properties of SiC powder synthesized by combustion synthesis. J Alloys Compd [Internet]. 2011 Jan;509(3):973–6. Available from: <URL>.

30. Cullity BD, Stock SR. Elements of X-ray Diffraction. USA: Prentice Hall; 2001.

31. Gardner J, Morrison FD. A-site size effect in a family of unfilled ferroelectric tetragonal tungsten bronzes: $Ba_4R_{0.67}Nb_{10}O_{30}$ (R= La, Nd, Sm, Gd, Dy and Y). Dalt Trans [Internet]. 2014;43(30):11687–95. Available from: <URL>.

32. Polyxeni V, Nikolaos D P, Nikos S, Sotirios X, Evangelos H. Temperature effects on grain growth phenomena and magnetic properties of silicon steels used in marine applications. Ann Mar Sci [Internet]. 2023 Jun 21;7(1):40–4. Available from: <URL>.

33. Güleryüz LF, İlhan M. Structural, morphological, spectral properties and high quantum efficiency of Eu^{3+}, B^{3+} co-activated double perovskite Ba_2GdMO_6 (M= Nb, Ta) phosphors. Mater Sci Eng B [Internet]. 2024 Jun;304:117373. Available from: <URL>.

34. Mahapatro J, Agrawal S. Effect of Eu3+ ions on electrical and dielectric properties of barium hexaferrites prepared by solution combustion method. Ceram Int [Internet]. 2021 Jul;47(14):20529–43. Available from: <URL>.

35. Evangeline T G, Annamalai A R, Ctibor P. Effect of Europium Addition on the Microstructure and Dielectric Properties of CCTO Ceramic Prepared Using Conventional and Microwave Sintering. Molecules [Internet]. 2023 Feb 8;28(4):1649. Available from: <URL>.

36. Esha IN, Al-Amin M, Toma FTZ, Hossain E, Khan MNI, Maria KH. Synthesis and analysis of the influence of Eu^{3+} on the structural, ferromagnetic, dielectric and conductive characteristics of $Ni_{0.4}Zn_{0.45}Cu_{0.15}Fe_{(2-x)}Eu_xO_4$ composites using conventional double sintering ceramic method. J Ceram Process Res [Internet]. 2019 Oct;20(5):530–9. Available from: <URL>.

37. Shah MR, Akther Hossain AKM. Structural and dielectric properties of La substituted polycrystalline $Ca(Ti_{0.5}Fe_{0.5})O_3$. Mater Sci [Internet]. 2013 Jan 25;31(1):80–7. Available from: <URL>.

38. Kadam AA, Shinde SS, Yadav SP, Patil PS, Rajpure KY. Structural, morphological, electrical and magnetic properties of Dy doped Ni–Co substitutional spinel ferrite. J Magn Magn Mater [Internet]. 2013 Mar;329:59–64. Available from: <URL>.

39. Tan YQ, Yu Y, Hao YM, Dong SY, Yang YW. Structure and dielectric properties of $Ba_5NdCu_{1.5}Nb_{8.5}O_{30-\delta}$ tungsten bronze ceramics. Mater Res Bull [Internet]. 2013 May;48(5):1934–8. Available from: <URL>.

40. Rayssi C, El.Kossi S, Dhahri J, Khirouni K. Frequency and temperature-dependence of dielectric permittivity and electric modulus studies of the solid solution $Ca_{0.85}Er_{0.1}Ti_{1-x}Co_{4x/3}O_3$ ($0 \le x \le 0.1$). RSC Adv [Internet]. 2018;8(31):17139–50. Available from: <URL>.

41. Wagner KW. Zur Theorie der unvollkommenen Dielektrika. Ann Phys [Internet]. 1913 Jan 14;345(5):817–55. Available from: <URL>.

42. Maxwell JC. A treatise on electricity and magnetism. London: Caleredon press, Oxford University; 1873.

43. Saengvong P, Chanlek N, Srepusharawoot P, Harnchana V, Thongbai P. Enhancing giant dielectric properties of Ta^{5+} -doped $Na_{1/2}Y_{1/2}Cu_3Ti_4O_{12}$ ceramics by engineering grain and grain boundary. J Am Ceram Soc [Internet]. 2022 May 15;105(5):3447–55. Available from: <URL>.

44. Karmakar S, Mohanty HS, Behera D. Exploration of alternating current conduction mechanism and dielectric relaxation with Maxwell–Wagner effect in NiO–CdO–Gd_2O_3 nanocomposites. Eur Phys J Plus [Internet]. 2021 Oct 15;136(10):1038. Available from: <URL>.

45. Samet M, Kallel A, Serghei A. Maxwell-Wagner-Sillars interfacial polarization in dielectric spectra of composite materials: Scaling laws and applications. J Compos Mater [Internet]. 2022 Aug 28;56(20):3197–217. Available from: <URL>.

46. Mach TP, Ding Y, Binder JR. Impact of Particle and Crystallite Size of $Ba_{0.6}Sr_{0.4}TiO_3$ on the Dielectric Properties of BST/P(VDF-TrFE) Composites in Fully

Printed Varactors. Polymers (Basel) [Internet]. 2022 Nov 19;14(22):5027. Available from: <URL>.

47. Kurnia, Heriansyah, Suharyadi E. Study on The Influence of Crystal Structure and Grain Size on Dielectric Properties of Manganese Ferrite ($MnFe_2O_4$) Nanoparticles. IOP Conf Ser Mater Sci Eng [Internet]. 2017 May;202:012046. Available from: <URL>.

48. Chi EO, Gandini A, Ok KM, Zhang L, Halasyamani PS. Syntheses, Structures, Second-Harmonic Generating, and Ferroelectric Properties of Tungsten Bronzes: $A_6M_2M'_8O_{30}$ (A= Sr^{2+}, Ba^{2+}, or Pb^{2+} ; M= Ti^{4+}, Zr^{4+}, or Hf^{4+} ; M'= Nb^{5+} or Ta^{5+}). Chem Mater [Internet]. 2004 Sep 1;16(19):3616–22. Available from: <URL>.

49. Rotaru A, Arnold DC, Daoud-Aladine A, Morrison FD. Origin and stability of the dipolar response in a family of tetragonal tungsten bronze relaxors. Phys Rev B [Internet]. 2011 May 31;83(18):184302. Available from: <URL>.

50. Neurgaonkar RR, Nelson JG, Oliver JR. Ferroelectric properties of the tungsten bronze $M^{2+}{}_6M^{4+}{}_2Nb_8O_{30}$ solid solution systems. Mater Res Bull [Internet]. 1992 Jun;27(6):677–84. Available from: <URL>.

51. Stennett MC, Reaney IM, Miles GC, Woodward DI, West AR, Kirk CA, et al. Dielectric and structural studies of $Ba_2MTi_2Nb_3O_{15}$ ($BMTNO_{15}$, M=Bi^{3+}, La^{3+}, Nd^{3+}, Sm^{3+}, Gd^{3+}) tetragonal tungsten bronze-structured ceramics. J Appl Phys [Internet]. 2007 May 15;101(10):104114. Available from: <URL>.

52. Li G, Cheng L, Liao F, Tian S, Jing X, Lin J. Luminescent and structural properties of the series $Ba_{6-x}Eu_xTi_{2+x}Ta_{8-x}O_{30}$ and $Ba_{4-y}K_yEu_2Ti_{4-y}Ta_{6+y}O_{30}$. J Solid State Chem [Internet]. 2004 Mar;177(3):875–82. Available from: <URL>.

53. Sati PC, Kumar M, Chhoker S, Jewariya M. Influence of Eu substitution on structural, magnetic, optical and dielectric properties of BiFeO3 multiferroic ceramics. Ceram Int [Internet]. 2015 Mar;41(2):2389–98. Available from: <URL>.

54. Ganguly P, Jha AK. Enhanced characteristics of $Ba_5SmTi_3Nb_7O_{30}$ ferroelectric nanocrystalline ceramic prepared by mechanical activation process: A comparative study. Mater Res Bull [Internet]. 2011 May;46(5):692–7. Available from: <URL>.

55. Kumar P, Kar M. Effect of structural transition on magnetic and optical properties of Ca and Ti co-substituted $BiFeO_3$ ceramics. J Alloys Compd [Internet]. 2014 Jan;584:566–72. Available from: <URL>.

56. Chakrabarti A, Bera J. Effect of La-substitution on the structure and dielectric properties of $BaBi_4Ti_4O_{15}$ ceramics. J Alloys Compd [Internet]. 2010 Sep;505(2):668–74. Available from: <URL>.

57. Fei Liu S, Jun Wu Y, Li J, Ming Chen X. Effects of oxygen vacancies on dielectric, electrical, and ferroelectric properties of $Ba_4Nd_2Fe_2Nb_8O_{30}$ ceramics. Appl Phys Lett [Internet]. 2014 Feb 24;104(8):082912. Available from: <URL>.

58. Kendall KR, Thomas JK, Loye HC. Synthesis and ionic conductivity of a new series of modified Aurivillius phases. Chem Mater [Internet]. 1995 Jan 1;7(1):50–7. Available from: <URL>.

59. İlhan M, Ekmekci MK, Esmer K. Structural and dielectric properties of Eu^{3+},B^{3+} co-doped $CoNb_2O_6$ ceramic. J Turkish Chem Soc Sect A Chem [Internet]. 2024 May 15;11(2):765–74. Available from: <URL>.

60. Chandra Sati P, Arora M, Chauhan S, Kumar M, Chhoker S. Effect of Dy substitution on structural, magnetic and optical properties of BiFeO3 ceramics. J Phys Chem Solids [Internet]. 2014 Jan;75(1):105–8. Available from: <URL>.

61. Nadeem M, Khan W, Khan S, Husain S, Ansari A. Tailoring dielectric properties and multiferroic behavior of nanocrystalline $BiFeO_3$ via Ni doping. J Appl Phys [Internet]. 2018 Oct 28;124(16):164105. Available from: <URL>.